

Fine-structure transitions of the carbon isoelectronic sequence C, N⁺ and O²⁺ induced by collisions with atomic hydrogen

Pei-Gen Yan,^{1*} James F. Babb,^{1†}

¹Center for Astrophysics | Harvard & Smithsonian, MS 14, 60 Garden St., Cambridge, MA 02138

24 November 2022

ABSTRACT

Fine-structure transitions can be involved in various processes including photon absorption, charge transfer and inelastic collision between ions, electrons and neutral atoms. We present fine-structure excitation and relaxation cross sections for the collisions of the first few members of the carbon isoelectronic sequence (C, N⁺ and O²⁺) with atomic hydrogen calculated using quantum-mechanical methods. For C, the scattering theory and computational approach is verified by comparison with previous calculations. The rate coefficients for the collisional processes are obtained. For N⁺ and O²⁺, the transitions correspond to the lines [O III] 52 μm, [O III] 88 μm, [N II] 122 μm, and [N II] 205 μm, observed in the far-infrared in the local Universe and more recently in high-redshift galaxies using radio interferometry. The influence of different potentials on the cross sections and rate coefficients are demonstrated.

Key words: ISM – molecular processes – scattering processes

1 INTRODUCTION

In many astrophysical environments, fine-structure levels of atoms and ions are populated by collisions with electrons, hydrogen atoms, and hydrogen molecules, as well as by photons. Excitation of an atom by such collisions might be followed by spontaneous emission leading to a loss of kinetic energy or “cooling.” The competition between relaxation of the fine-structure levels by collisions and spontaneous emission affects the diagnostic potential of the observed lines. Cross sections and rate coefficients for collisional relaxation can be calculated and used in sophisticated modeling codes to interpret astronomical observations.

In the far-infrared, the lines [O I] 63 μm, [O I] 146 μm, and [C II] 158 μm are commonly observed and utilized as probes of physical conditions; accordingly the collisions of O and C⁺ with electrons, hydrogen atoms, and hydrogen molecules are well-studied. Recently, the rest-frame far-infrared lines [O III] 52 μm, [O III] 88 μm, [N II] 122 μm, and [N II] 205 μm, became of interest¹ in observations of high-redshift galaxies ($z > 6$) using ALMA, see, for example, Inoue et al. (2014), Sugahara et al. (2021), and Ramos Padilla et al. (2022). While the O²⁺ and N⁺ lines above generally trace H II regions and thus are expected to be most affected by electron collisions—for which collision strengths are available, see Tayal (2011); Tayal & Zatsarinny (2017)—complete interpretations of these nascent high- z observations are still in their infancy and as far as we know, no data on the collisional cross sections and rate coefficients for fine-structure excitation or de-excitation of N⁺ or O²⁺ in collisions with H are available should they be needed for modeling or simulation. In

the present paper, we treat the collisions

$$A(^3P_j) + H(^2S_{1/2}) \rightarrow A(^3P_{j'}) + H(^2S_{1/2}), \quad (1)$$

where A can be C, N⁺ and O²⁺ and (j, j') can be (1, 2), (0, 1), or (0, 2). For ground state carbon atoms, quantum-mechanical calculations of cross sections for process (1) were previously reported by Launay & Roueff (1977) and Abrahamsson et al. (2007). Although the atomic structure of the ions is in some ways similar to neutral carbon we find that in collisions with hydrogen atoms the resulting cross sections and rate coefficients have quantitative differences.

2 THEORETICAL MODELS

We use a close-coupling scattering formulation (Mies 1973; Launay & Roueff 1977) with the wave function Φ^{JM} expanded in the space-fixed basis $|j_a j_b j_{ab} l J M\rangle$ as

$$\Phi^{JM} = \sum_{j_{ab}, l} F_{j_{ab} l}^{JM}(R) |j_a j_b j_{ab} l J M\rangle, \quad (2)$$

where the two colliding systems are labeled a and b , $F_{j_{ab} l}^{JM}(R)$ is the reduced radial wave function, R is the internuclear distance, $j_{ab} = j_a + j_b$ is the total electric angular momentum, and $J = j_{ab} + l$ is the total angular momentum. With the total wave function (Eq. 2), the Schrödinger equation that describes the internal motions of the C, N⁺ or O²⁺ ion and H system can be reduced to a set of coupled differential equations, expressed in atomic units (a.u.) as

$$\left[\frac{d}{dR^2} - \frac{l(l+1)}{R^2} + k_{j_a}^2 \right] F_{j_{ab} l}^J(R) = 2\mu \sum_{j'_a j'_b l'} U_{j_a j_{ab} l; j'_a j'_{ab} l'} F_{j_{ab} l}^J(R), \quad (3)$$

with the wave number k_{j_a} defined by $k_{j_a}^2 = 2\mu(E - \varepsilon_{j_a})$, where μ is the reduced mass of systems a and b , E is the total collision energy,

* E-mail: peigen.yan@cfa.harvard.edu

† E-mail: jbabb@cfa.harvard.edu

¹ For completeness, we note that [N III] 57 μm is of interest, but we do not treat it in this paper.

and ε_{j_a} is the fine-structure state splitting energy of the C, N⁺, or O²⁺ atom. We adopt the values of ε_{j_a} from NIST (Kramida et al. 2022): For the C atom

$$\varepsilon_0 = 0, \quad \varepsilon_1 = 16.417 \text{ cm}^{-1}, \quad \varepsilon_2 = 43.413 \text{ cm}^{-1}, \quad (4)$$

for the N⁺ ion,

$$\varepsilon_0 = 0, \quad \varepsilon_1 = 48.7 \text{ cm}^{-1}, \quad \varepsilon_2 = 130.8 \text{ cm}^{-1}. \quad (5)$$

and for the O²⁺ ion,

$$\varepsilon_0 = 0, \quad \varepsilon_1 = 113.178 \text{ cm}^{-1}, \quad \varepsilon_2 = 306.174 \text{ cm}^{-1}. \quad (6)$$

U is the coupling matrix given by the summation of the V_{el} and V_{so} matrices in the basis $|j_a j_b j_{ab} l J M\rangle$. The V_{so} matrix is diagonal and the nonzero elements are the fine-structure splittings that are given above in (4), (5), or (6). For the elements of the potential energy V_{el} matrix, we adopt the expression described in Launay & Roueff (1977); Flower et al. (2000); Krems et al. (2006). Then the cross sections for fine-structure transitions are calculated by

$$\sigma_{j_a \rightarrow j'_a}(E) = \sum_J \sigma_{j_a \rightarrow j'_a}^J(E), \quad (7)$$

$$\sigma_{j_a \rightarrow j'_a}^J(E) = \frac{\pi}{k_{j_a}^2} \frac{2J+1}{(2j_a+1)(2j_b+1)} \sum_{j_{ab} l j'_{ab} l'} |T_{j_a j'_a b l' : j_a j_{ab} l}^J|^2, \quad (8)$$

where $\sigma_{j_a \rightarrow j'_a}^J$ are the partial cross sections and the T matrix is defined by $T^J = -2iK^J(I - iK^J)^{-1}$, where K^J is the open channel reaction matrix defined in Johnson (1973). The maximum value for the partial waves J is set as 1000 and for the maximum collision energy used (9.05 eV), the partial cross section converged for CH at about 300, for NH⁺ at about 500, and for OH²⁺ at about 990.

3 INTERATOMIC POTENTIALS

For the CH system, the four electronic states involved in the fine-structure transitions of C(³P) in collisions with H(²S) are the b⁴Π, B²Σ⁻, a⁴Σ⁻, and X²Π states. The present calculations, using the MRCI-DKH (Douglas-Kroll-Hess) method with the aug-cc-pV5Z-dk basis within MOLPRO 2010.1 (Werner et al. 2010), are shown in Fig. 1. The calculated potential energies were smoothly joined to the long-range potential function $-C_6/R^6$ at $R = 9a_0$, where we used the value $C_6 = 20.3$ a.u. (Yau & Dalgarno 1976).

For the NH⁺ system, the four electronic states involved in the fine-structure transitions of N(³P) in collision with H(²S) are the 2⁴Σ⁻, 1⁴Π, 1²Σ⁻, and X²Π states. The present calculations, using the MRCI-DKH (Douglas-Kroll-Hess) method with the aug-cc-pV5Z-dk basis within MOLPRO 2010.1 (Werner et al. 2010), are shown in Fig. 2, along with the 1⁴Σ⁻ state correlating to N(⁴S) + H(¹S). The potentials were joined at $R = 17a_0$ to the long-range charge-induced dipole interaction $-\alpha_{\text{H}}/2R^4$ between N(³P) and H(²S), where $\alpha_{\text{H}} = 4.5$ a.u. is the polarizability of the hydrogen atom.

For the OH²⁺ system, the four electronic states that are involved in the fine-structure transitions of O²⁺(³P) in collision with H(²S) are the 3²Π, 2²Σ⁻, 2⁴Π, and 3⁴Σ⁻ states. We adopted the recent MRCI+Q calculations using the aug-cc-pV5Z basis that were presented by De Melo et al. (2021) and which we show in Fig. 3. The long-range charge-induced dipole interaction potential $-\alpha_{\text{H}}/R^4$ between O²⁺(³P) ion and the H(²S) atom was smoothly connected to the potentials at $R = 20a_0$.

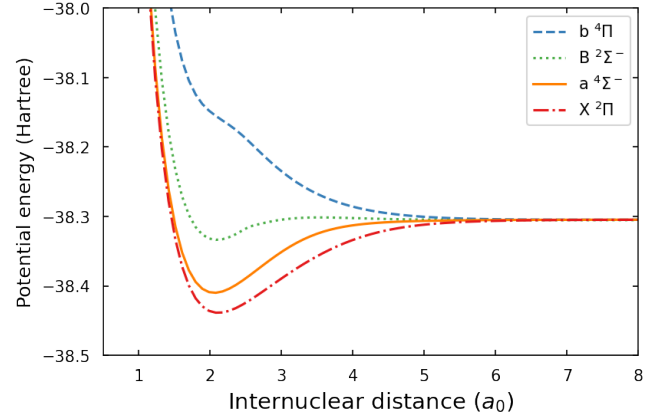


Figure 1. Potential energies (in Hartrees) for the CH system as functions of the internuclear distance R (in a_0) labeled from the top down at the equilibrium distance of the lowest state: b⁴Π (blue dashed line), B²Σ⁻ (green dotted line), a⁴Σ⁻ (orange solid line) and X²Π (red dashdot line).

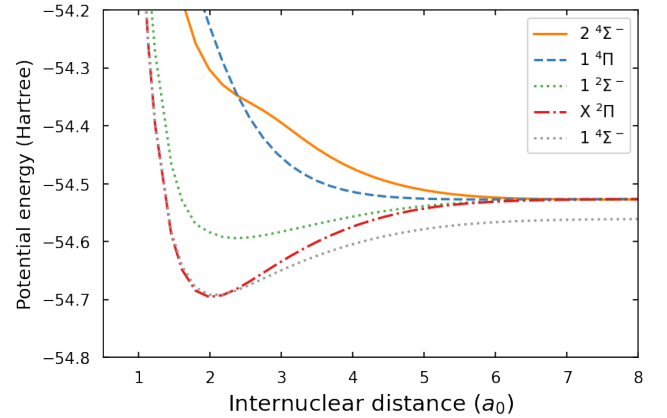


Figure 2. Potential energies for the NH⁺ system as functions of the internuclear distance R . The 1⁴Σ⁻ state correlating to N(⁴S)–H(¹S) is labeled with the gray dotted line. The other states correlate to N(³P)–H(²S) and are labeled from the top down at the equilibrium distance of the lowest state: 1⁴Π (blue dashed line), 2⁴Σ⁻ (orange solid line), 1²Σ⁻ (green dotted line) and X²Π (red dashdot line).

4 SCATTERING CALCULATIONS

Using the theoretical quantum description of a collision between two open-shell atoms in arbitrary angular momentum states derived by Krems et al. (2006), the scattering calculations were performed using a Python code that we wrote based partially on the MOLCOL Fortran 77 code (Flower et al. 2019) utilizing Johnson's multichannel logarithmic derivative algorithm (Johnson 1973). In order to prove the reliability of the present approach, the Python code was tested by calculating cross sections for the C⁺-H, the Si⁺-H, and the O-H systems (Yan & Babb 2022b); in all these cases, the corresponding rate coefficients were found to be in very good agreement with those of preceding calculations from the literature when we used the potential energy data of the original sources. In the following, we will also show that our calculations of the cross sections and rate coefficients for the C-H system are in good accord with those of others.

Having established the reliability of our theory and code, the cross

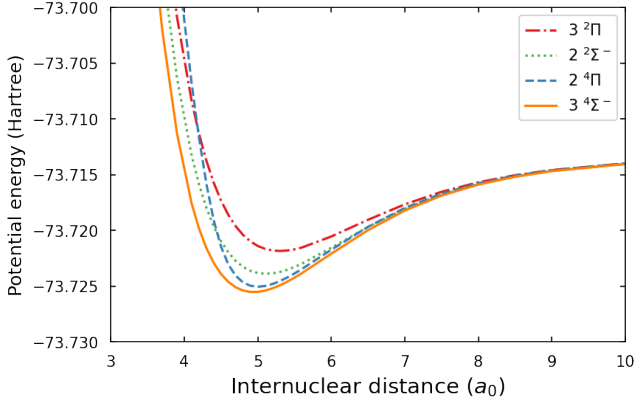


Figure 3. Potential energies for the OH^{2+} system as functions of the internuclear distance R , labeled from the top down at the equilibrium distance of the lowest state: $3^2\Pi$ (red dashdot line), $2^2\Sigma^-$ (green dotted line), $2^4\Pi$ (blue dashed line), and $3^4\Sigma^-$ (orange solid line) from De Melo et al. (2021).

sections were computed for collisional energies up to about 8.6 eV. The scattering equations were integrated from $R = 1 a_0$ to $R = 30 a_0$. The corresponding excitation and relaxation rate coefficients were computed for temperatures up to 10,000 K by averaging over a Maxwellian energy distribution,

$$k_{j_a \rightarrow j'_a}(T) = \left(\frac{8}{\pi \mu k_B^3 T^3} \right)^{1/2} \int_0^\infty \sigma_{j_a \rightarrow j'_a}(E_k) e^{-E_k/k_B T} E_k dE_k, \quad (9)$$

where T is the temperature, k_B is Boltzmann's constant, σ is the cross section, and E_k is the kinetic energy.

5 RESULTS

With the CH potentials as described above, the calculated excitation and relaxation cross sections² are shown in Fig. 4. The corresponding rate coefficients as functions of temperature are given in Fig. 5 and Table 1. From Fig. 5, we see that at low temperatures (or relatively small kinetic energies), the excitation rate coefficient of the $0 \rightarrow 1$ transition is larger than those of the $1 \rightarrow 2$ and $0 \rightarrow 2$ transitions. The energy differences of the $0 \rightarrow 1$ transition are the smallest leading to this being the strongest transition. With increasing temperature (kinetic energy), we find that the rate coefficients for the $0 \rightarrow 1$ transition drop to being the smallest, such behavior is explained by the “forbidden” selection rules demonstrated by Monteiro & Flower (1987). This “forbidden” selection rule may explain the lower relaxation rate coefficients of $2 \rightarrow 0$ and $1 \rightarrow 0$ transitions compared to that of the $2 \rightarrow 1$ transition. In order to further prove the reliability of the present approach, we also made comparisons of the present calculations with those of Launay & Roueff (1977) and of Abrahamsson et al. (2007), as shown in Fig. 6. It can be seen that the present calculations are in good agreement with the other works, especially for the $0 \rightarrow 1$ transitions. The discrepancies for the rate

² Note that the cross sections correspond strictly to the process (1) and we calculate these to energies $\sim 10^5$ K to have a suitable integrand for the rate coefficient of Eq. (9). In a gas of temperature $\sim 10,000$ K or higher cross sections corresponding to other channels such as $C(^1D)$ and $C(^1S)$ might be opened.

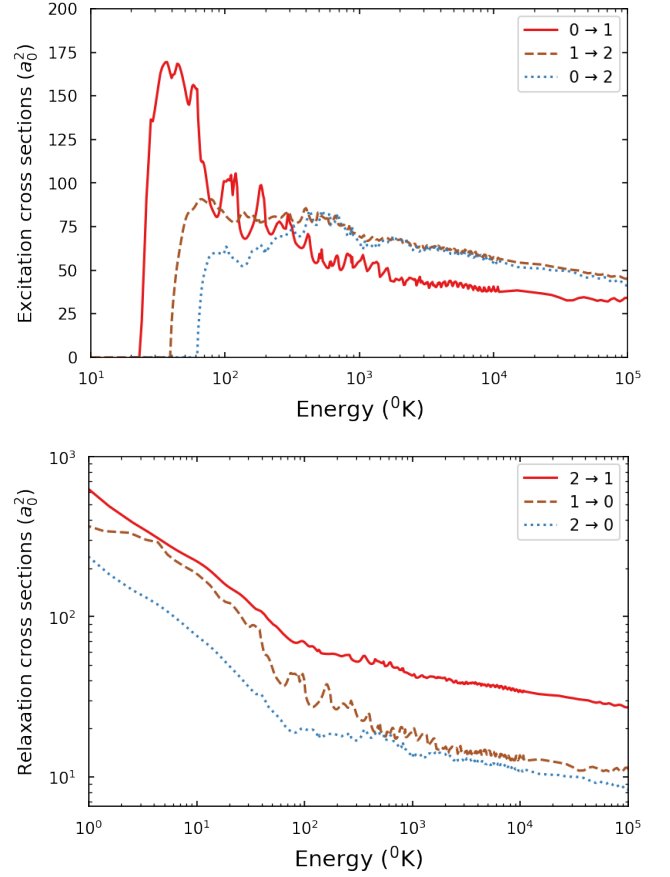


Figure 4. Excitation and relaxation cross sections for fine-structure transitions of C in collision with H. The three transitions ($j \rightarrow j'$) are labeled with different colors.

coefficients of the $1 \rightarrow 2$ and $0 \rightarrow 2$ transitions could be caused by the different potentials we used. Comparing Figs. 4 and 5, it is apparent that the relaxation cross sections decrease as a function of energy, while the relaxation rate coefficients increase as a function of temperature, a consequence of the energy dependence in the integrand of Eq. (9). For example, the log-log plot of Fig. 4 shows that the relaxation cross sections decrease slowly for energy $E_k > 1000^0\text{K}$ and thus the relaxation rate coefficients shown in Fig. 5 increase for $T > 100$ K.

With the NH^+ potentials as described above, the calculated excitation and relaxation cross sections are shown in Fig. 7. The corresponding rate coefficients for the fine structure transitions of N^+ in collision with H as a function of temperature are given in Fig. 8 and Table 2. Compared to the CH system, the cross sections and rate coefficients of the $1 \rightarrow 2$ and $0 \rightarrow 2$ transitions for the NH^+ system are larger because of the stronger long-range attractions and deeper potential wells as shown in Fig. 2. Furthermore, we find that for NH^+ the $1 \rightarrow 2$ transition rate coefficient is the largest compared to CH where the $0 \rightarrow 2$ transition is the largest. This phenomenon might be caused by the different shapes of the potentials for the two systems: The $1^4\Sigma^-$ state of the CH system has a much deeper well than the $2^4\Sigma^-$ state of the NH^+ system. Similarly to the CH system, the excitation rate coefficients of the $0 \rightarrow 1$ transition are also the smallest among the three transitions because of the “forbidden” selection rule. N^+ can be removed by the exothermic charge transfer process (Butler

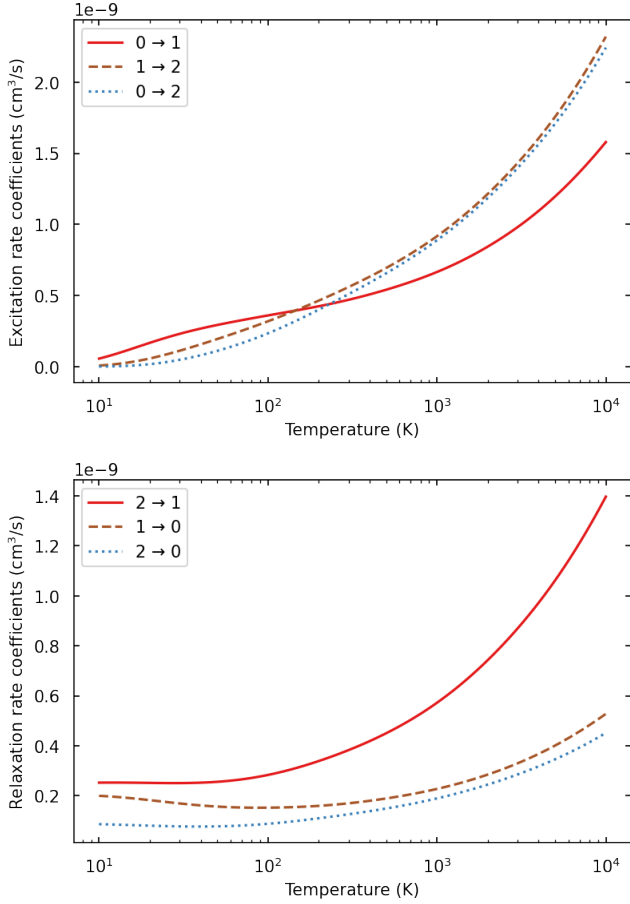


Figure 5. Excitation and relaxation rate coefficients for fine-structure transitions of C in collision with H. The three transitions ($j \rightarrow j'$) are labeled with different colors.

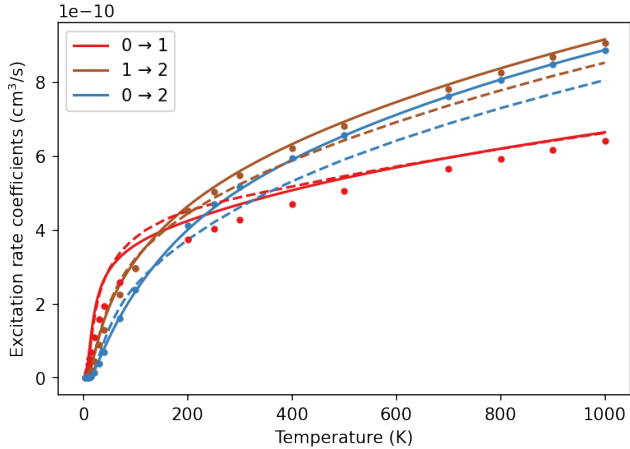


Figure 6. Comparison of temperature dependent excitation rate coefficients of the present calculations (solid lines) with those of Abrahamsson et al. (2007) (large dots) and with those of Launay & Roueff (1977) (dashed lines).

Table 1. Rate coefficients (in units of $10^{-9} \text{ cm}^3 \text{ s}^{-1}$) for the fine-structure excitation and relaxation of $\text{C}(^3P_j)$ by H.

T (K)	$j = 0 \rightarrow j' = 1$	$j = 0 \rightarrow j' = 2$	$j = 1 \rightarrow j' = 2$
100	0.360	0.234	0.319
200	0.425	0.401	0.465
500	0.540	0.656	0.693
700	0.596	0.762	0.794
1000	0.665	0.888	0.917
2000	0.844	1.185	1.215
5000	1.195	1.707	1.755
7000	1.368	1.948	2.010
10000	1.579	2.242	2.320
T (K)	$j = 1 \rightarrow j' = 0$	$j = 2 \rightarrow j' = 0$	$j = 2 \rightarrow j' = 1$
10	0.199	0.086	0.252
20	0.182	0.080	0.251
50	0.157	0.077	0.256
70	0.153	0.081	0.265
100	0.152	0.088	0.283
200	0.159	0.110	0.339
500	0.189	0.149	0.450
700	0.205	0.167	0.504
1000	0.227	0.189	0.572
2000	0.284	0.245	0.743
5000	0.400	0.346	1.061
7000	0.458	0.393	1.213
10000	0.527	0.451	1.397

Table 2. Rate coefficients (in units of $10^{-9} \text{ cm}^3 \text{ s}^{-1}$) for the fine-structure excitation and relaxation of $\text{N}^+(^3P_j)$ by H.

T (K)	$j = 0 \rightarrow j' = 1$	$j = 0 \rightarrow j' = 2$	$j = 1 \rightarrow j' = 2$
100	0.466	0.153	0.298
200	0.613	0.475	0.626
500	0.742	1.072	1.116
700	0.793	1.306	1.305
1000	0.856	1.558	1.514
2000	0.998	2.093	1.973
5000	1.228	3.002	2.764
7000	1.353	3.408	3.126
10000	1.524	3.878	3.556
T (K)	$j = 1 \rightarrow j' = 0$	$j = 2 \rightarrow j' = 0$	$j = 2 \rightarrow j' = 1$
10	0.353	0.169	0.458
20	0.333	0.156	0.461
50	0.330	0.171	0.513
70	0.324	0.184	0.544
100	0.314	0.201	0.583
200	0.290	0.244	0.678
500	0.285	0.313	0.848
700	0.292	0.342	0.927
1000	0.306	0.376	1.022
2000	0.345	0.460	1.256
5000	0.415	0.624	1.698
7000	0.455	0.700	1.907
10000	0.511	0.790	2.158

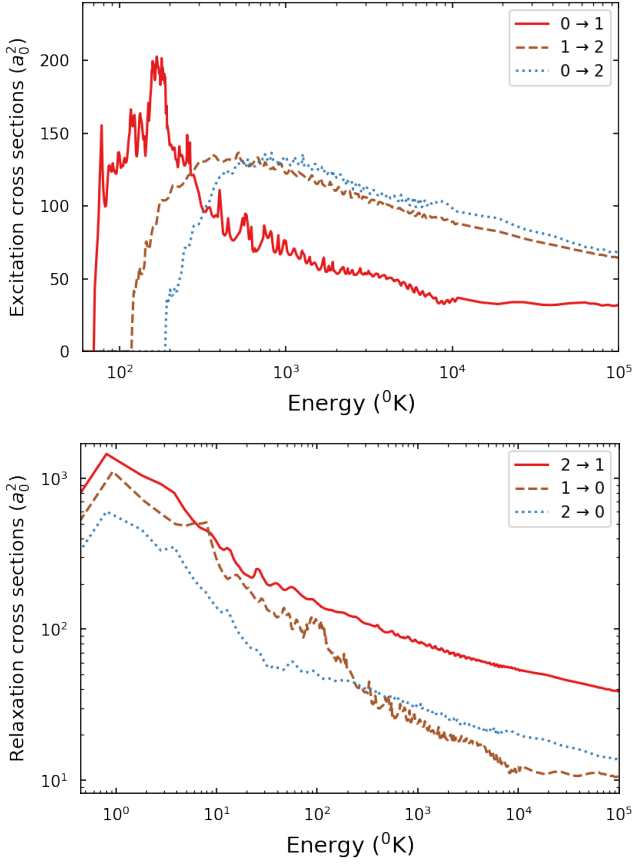
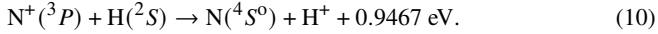


Figure 7. Excitation and relaxation cross sections for fine-structure transitions of N^+ in collision with H . The three transitions ($j \rightarrow j'$) are labeled with different colors.

& Dalgarno 1979)



The rate coefficients were calculated by Lin et al. (2005) and they decrease from a value of about $10^{-13} \text{ cm}^3/\text{s}$ at 10,000 K and appear to be considerably slower than the relaxation process which is no less than $10^{-10} \text{ cm}^3/\text{s}$ even at 10 K.

With the OH^{2+} potentials as described above, the calculated cross sections for fine structure transition of O^{2+} in collision with H are shown in Fig. 9. The corresponding rate coefficients are given in Fig. 10 and Table 3. From Figs. 9 and 10, we see that at the lowest temperatures both the cross sections and rate coefficients of the OH^{2+} system are larger than those of the CH and NH^+ systems. This is caused by the stronger long-range interaction $-\alpha_H/R^4$ of the OH^{2+} system compared to the other two systems. The four wells of the OH^{2+} potentials, see Fig. 3, lead to the mild increase of the $0 \rightarrow 1$ transition for temperatures larger than 4000 K. O^{2+} can be removed by the charge transfer process (Butler et al. 1979)



The rate coefficient is about $10^{-9} \text{ cm}^3/\text{s}$ over the temperature range $200 < T < 10,000 \text{ K}$ (Honvault et al. 1995), which is comparable to our calculated fine-structure relaxation rate coefficients shown in Table 3. This might be an important consideration for modeling applications.

The critical density n_c , an important parameter to indicate whether

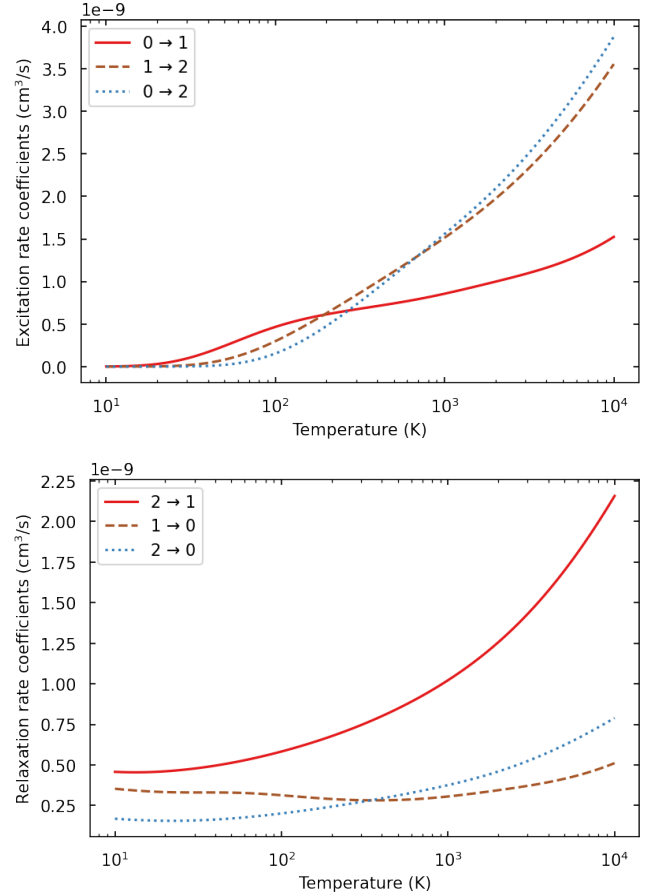


Figure 8. Excitation and relaxation rate coefficients for fine-structure transitions of N^+ in collision with H . The three transitions ($j \rightarrow j'$) are labeled with different colors.

collisions affect the presence of fine structure lines, is defined as

$$n_c(j; T; x) = \frac{\sum_{j'} A(j \rightarrow j')}{\sum_{j'} k_{j \rightarrow j'}(T; x)}, \quad (12)$$

where $A(j \rightarrow j')$ is the transition probability (Mendoza 1983) and $k_{j \rightarrow j'}(T; x)$ is the relaxation rate coefficient for collisions with species x , which may be hydrogen (H) or electrons (e). Our calculated critical densities for N^+ and O^{2+} , respectively, and H are shown in Figs. 11 and 12. We also plot the critical densities for electrons (e), which were determined using the effective collision strengths from Tayal (2011) for N^+ and from Tayal & Zatsarinny (2017) for O^{2+} . The graphical data in Figs. 11 and 12 might be useful for considerations of the relative importance of hydrogen and electron densities at specific temperatures. For example, we can see that the critical densities induced by electrons are 10 to 10^2 times smaller than those induced by hydrogen atoms due to the strong electron-ion interactions.

6 CONCLUSION

We introduced a methodology that yields consistent sets of rate coefficients for a number of cases. Based partially on the MOLCOL Fortran code (Flower et al. 2019), we developed a new Python code utilizing Johnson's multichannel logarithmic derivative algorithm

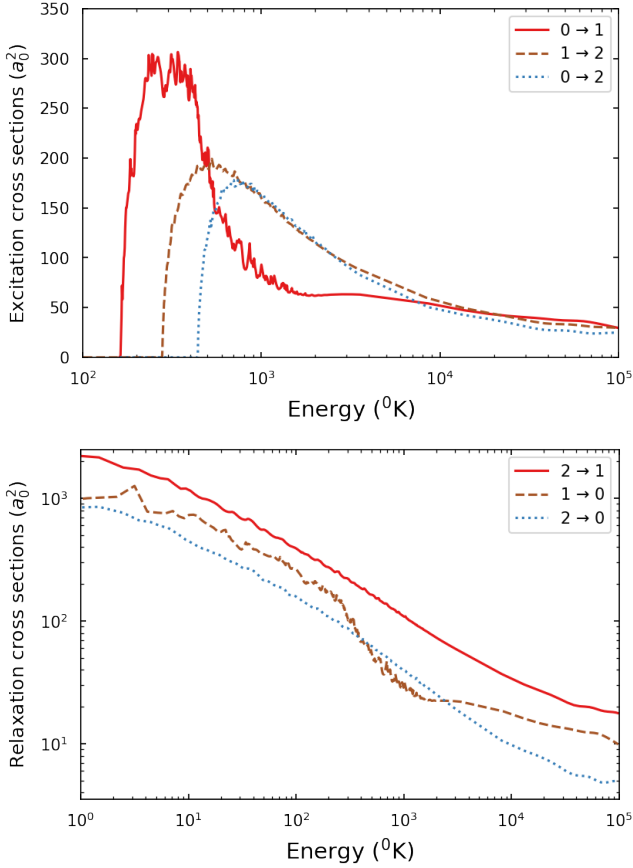


Figure 9. Excitation and relaxation cross sections for fine-structure transitions of O^{2+} in collision with H. The three transitions ($j \rightarrow j'$) are labeled with different colors.

(Johnson 1973). We presented for the first time a comparison of the excitation and relaxation cross sections and rate coefficients for fine-structure transitions in collision of C, N^+ , or O^{2+} and atomic hydrogen. The calculations are based on accurate CH (present work), NH^+ (present work), and OH^{2+} (De Melo et al. 2021) potentials. The present research may be useful in applications of far-infrared lines to astrophysical diagnostics.

DATA AVAILABILITY

The data points corresponding to the rate coefficients plotted in Figs. 8 and 10 are given in LAMDA format (Schöier et al. 2005) at Figshare (Yan & Babb 2022a).

ACKNOWLEDGEMENTS

This work was supported by NASA APRA grant 80NSSC19K0698.

REFERENCES

- Abrahamsson E., Krems R. V., Dalgarno A., 2007, *ApJ*, 654, 1171
 Butler S. E., Dalgarno A., 1979, *ApJ*, 234, 765
 Butler S. E., Bender C. F., Dalgarno A., 1979, *ApJ*, 230, L59
 De Melo G. F., Franzreb K., Ornellas F. R., 2021, *PCCP*, 23, 13672

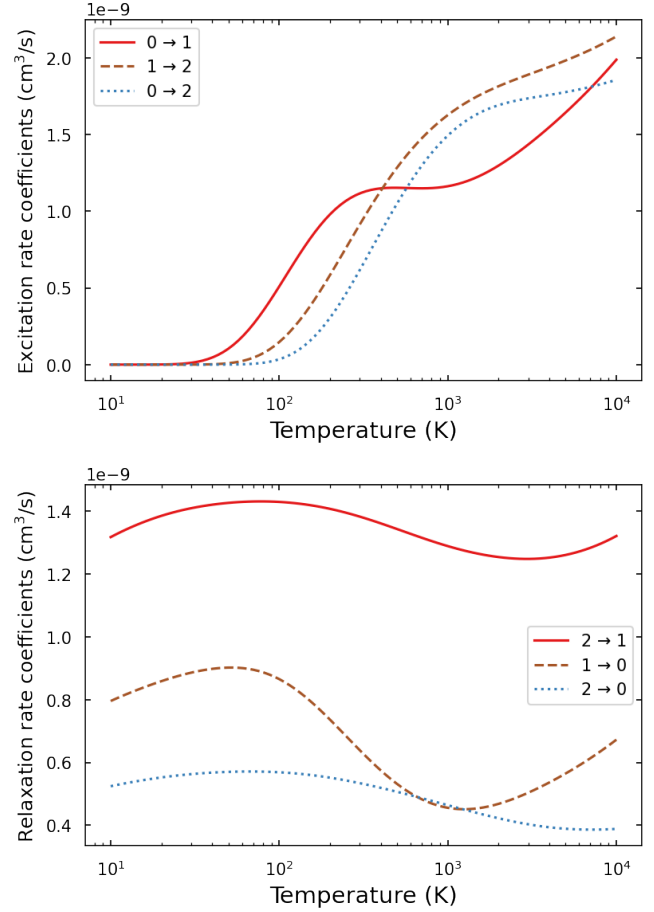


Figure 10. Excitation and relaxation rate coefficients for fine-structure transitions of O^{2+} in collision with H. The three transitions ($j \rightarrow j'$) are labeled with different colors.

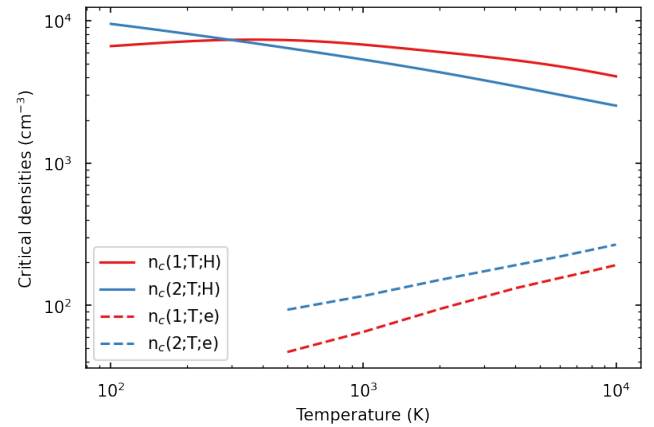
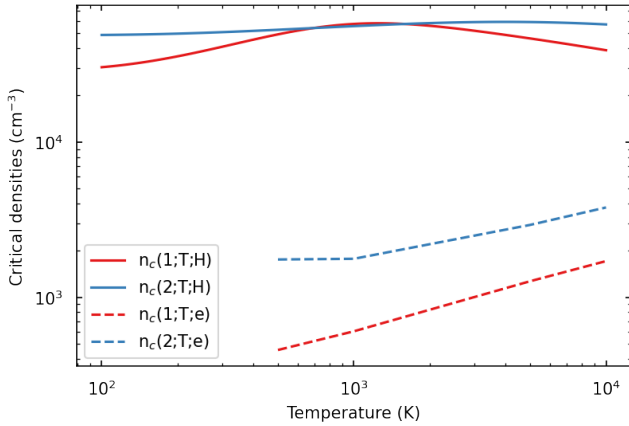


Figure 11. Critical densities for the relaxation of N^+ in collision with hydrogen (solid lines) and electrons (dashed lines). For electrons, data from Tayal (2011) were used.

Table 3. Rate coefficients (in units of $10^{-9} \text{ cm}^3\text{s}^{-1}$) for the fine-structure excitation and relaxation of $O^{2+}(^3P_j)$ by H .

T (K)	$j = 0 \rightarrow j' = 1$	$j = 0 \rightarrow j' = 2$	$j = 1 \rightarrow j' = 2$
100	0.510	0.348	0.147
200	0.979	0.305	0.583
500	1.152	1.050	1.284
700	1.149	1.296	1.474
1000	1.162	1.493	1.626
2000	1.296	1.690	1.814
5000	1.643	1.776	1.982
7000	1.800	1.809	2.051
10000	1.987	1.856	2.138

T (K)	$j = 1 \rightarrow j' = 0$	$j = 2 \rightarrow j' = 0$	$j = 2 \rightarrow j' = 1$
10	0.796	0.525	1.318
20	0.859	0.552	1.386
50	0.902	0.570	1.427
70	0.896	0.571	1.431
100	0.866	0.569	1.430
200	0.737	0.552	1.408
500	0.532	0.507	1.344
700	0.483	0.486	1.316
1000	0.456	0.464	1.288
2000	0.469	0.421	1.249
5000	0.566	0.387	1.255
7000	0.614	0.384	1.279
10000	0.673	0.387	1.318


Figure 12. Critical densities for the relaxation of O^{2+} in collision with hydrogen (solid lines) and electrons (dashed lines). For electrons, data from [Tayal & Zatsarinny \(2017\)](#) were used.

- Flower D., Bourhis G., Launay J.-M., 2000, *Comput. Phys. Commun.*, 131, 187
- Flower D., Bourhis G., Launay J.-M., 2019, MOLCOL: A program for solving atomic and molecular collision problems, doi:10.17632/NRHFXT7G69.1, <https://data.mendeley.com/datasets/nrhfxt7g69/1>
- Honvault P., Gargaud M., Bacchus-Montabonel M. C., McCarroll R., 1995, *A&A*, 302, 931
- Inoue A. K., Shimizu I., Tamura Y., Matsuo H., Okamoto T., Yoshida N., 2014, *ApJ*, 780, L18
- Johnson B., 1973, *J. Comp. Phys.*, 13, 445
- Kramida A., Yu. Ralchenko Reader J., and NIST ASD Team 2022, NIST Atomic Spectra Database (ver. 5.10), [Online]. Available:

- <https://physics.nist.gov/asd> [2022, October 25]. National Institute of Standards and Technology, Gaithersburg, MD.
- Krems R. V., Jamieson M. J., Dalgarno A., 2006, *ApJ*, 647, 1531
- Launay J. M., Roueff E., 1977, *A&A*, 56, 289
- Lin C. Y., Stancil P. C., Gu J. P., Buenker R. J., Kimura M., 2005, *Phys. Rev. A*, 71, 062708
- Mendoza C., 1983, *IAU Symp.*, 103, 143
- Mies F. H., 1973, *Phys. Rev. A*, 7, 942
- Monteiro T. S., Flower D. R., 1987, *MNRAS*, 228, 101
- Ramos Padilla A. F., Wang L., van der Tak F. F. S., Trager S., 2022 ([arXiv:2205.11955](https://arxiv.org/abs/2205.11955))
- Schöier F. L., van der Tak F. F. S., van Dishoeck E. F., Black J. H., 2005, *A&A*, 432, 369
- Sugahara Y., et al., 2021, *ApJ*, 923, 5
- Tayal S. S., 2011, *ApJS*, 195, 12
- Tayal S. S., Zatsarinny O., 2017, *ApJ*, 850, 147
- Werner H.-J., Knowles P. J., Knizia G., Manby F. R., Schütz M., et al., 2010, MOLPRO, version 2010.1, a package of *ab initio* programs
- Yan P.-G., Babb J. F., 2022a, Figshare, doi:10.6084/m9.figshare.21256365
- Yan P.-G., Babb J. F., 2022b, *RNAAS*, 6, 145
- Yau A. W., Dalgarno A., 1976, *ApJ*, 206, 652